COMMUNICATIONS PHYSICS

ARTICLE

https://doi.org/10.1038/s42005-020-0381-8 OPEN

Electrical nucleation, displacement, and detection of antiferromagnetic domain walls in the chiral antiferromagnet Mn_3Sn

Satoshi Sugimoto[1,2,3], Yoshinobu Nakatani[4], Yuta Yamane[5,6], Muhammad Ikhlas[1], Kouta Kondou[2], Motoi Kimata[7], Takahiro Tomita[1], Satoru Nakatsuji[1,8,9,10] & Yoshichika Otani[1,2,8,10]✉

Antiferromagnets exhibiting distinctive responses to the electric and magnetic fields have attracted attention as breakthrough materials in spintronics. The current-induced Néel-order spin-orbit torque can manipulate the antiferromagnetic domain wall (AFDW) in a collinear CuMnAs owing to a lack of local inversion symmetry. Here, we demonstrate that the electrical nucleation, displacement, and detection of AFDWs are also possible in a noncollinear antiferromagnet, i.e., chiral Mn_3Sn with local inversion symmetry. The asymmetric magnetoresistance measurements reveal that AFDWs align parallel to the kagome planes in the microfabricated wire. Numerical calculation shows these AFDWs consist of stepwise submicron size Bloch wall-like spin textures in which the octupole moment gradually rotates over three segments of domain walls. We further observed that the application of a pulse-current drives these octupole based AFDWs along the wire. Our findings could provide a guiding principle for engineering the AFDW structure in the chiral antiferromagnetic materials.

[1] Institute for Solid State Physics, University of Tokyo, 5-1-5 Kashiwanoha, Kashiwa 277-8581, Japan. [2] Center for Emergent Matter Science, RIKEN, 2-1 Hirosawa, Wako 351-0198, Japan. [3] Research Center for Magnetic and Spintronic Materials, National Institute for Materials Science (NIMS), 1-2-1 Sengen, Tsukuba 305-0047, Japan. [4] Department of Computer Science, University of Electro-Communications, 1-5-1 Chofugaoka, Chofu-Shi, Tokyo 182-8585, Japan. [5] Frontier Research Institute for Interdisciplinary Sciences, Tohoku University, 6-3 Aramaki Aza Aoba, Aoba-Ku, Sendai 980-0845, Japan. [6] Laboratory for Nanoelectronics and Spintronics, Research Institute of Electrical Communication, Tohoku University, 2-1-1 Katahira, Aoba-Ku, Sendai 980-8577, Japan. [7] Institute for Materials Research, Tohoku University, 2-1-1 Katahira, Aoba-Ku, Sendai 980-8577, Japan. [8] CREST, Japan Science and Technology Agency (JST), 4-1-8 Honcho Kawaguchi, Saitama 332-0012, Japan. [9] Department of Physics, University of Tokyo, Hongo, Bunkyo-KuTokyo 113-0033, Japan. [10] Trans-scale Quantum Science Institute, University of Tokyo, Hongo, Bunkyo-KuTokyo 113-0033, Japan. ✉email: yotani@issp.u-tokyo.ac.jp

Electrical manipulation of the magnetic domain[1–3] is the essential technology for spintronics. In recent years, antiferromagnetic spintronics[4] has attracted considerable interest because of various advantages, such as negligible stray fields and fast spin dynamics in the frequency range of subterahertz. It has, however, been challenging to control magnetic states of antiferromagnets by electrical means due to zero spontaneous magnetization, and weak magnetic susceptibilities in magnetic fields. The recent demonstration of field-like, Néel-order spin–orbit torque in collinear antiferromagnets with local inversion asymmetry[5], CuMnAs[6,7], and Mn_2Au[8], led to the breakthrough in the antiferromagnetic spintronics. These works have revealed a promising potential for electrical manipulation of antiferromagnetic domain walls (AFDWs) and paved the way for the use of antiferromagnets as well as ferromagnets for memory device applications.

Besides, the new class of noncollinear chiral antiferromagnet, Mn_3Sn, has currently attracted a great deal of attention owing to its intriguing electronic properties. Mn_3Sn has a hexagonal kagome lattice structure with a space group, $P6_3/mmc$[9], recently discovered as a magnetic Weyl semimetal[10]. Despite vanishingly small magnetization[11–13], the inverse triangular chiral antiferromagnetic phase of Mn_3Sn below 430 K shows unusual transport properties, such as a substantial anomalous Hall effect (AHE)[14,15], giant anomalous Nernst effect[16], strong anisotropic magnetoconductance[10], and magnetic spin Hall effect[17]. These properties originate from the macroscopic breaking of time-reversal symmetry (TRS) associated with the noncollinear antiferromagnetic order. A recent theory by Suzuki et al.[18] has clarified that it is a ferroic order of a cluster magnetic octupole that breaks TRS. Higo et al.[19] performed the magneto-optical Kerr effect (MOKE) measurements and succeeded in demonstrating the presence of the TRS-broken magnetic octupolar domains and domain walls.

Figure 1a, b shows the crystal structure and cluster magnetic octupole in Mn_3Sn. The cluster octupole moment resides on hexagonally located six Mn atoms between neighboring kagome planes $z = 0$ and $z = 1/2$ as enclosed by blue lines in Fig. 1a, and has six spin configurations labeled by $\alpha\pm$, $\beta\pm$, and $\gamma\pm$ domains indicated in Fig. 1b[18,20]. For instance, the $\alpha+$ domain contains the magnetic structure characterized by the octupole moment, which breaks TRS, and induces a very small remanent magnetization (~2 $m\mu_B$ per Mn) along the octupole, $[2\bar{1}\bar{1}0]$ direction (blue arrow in Fig. 1b). In the same manner, the cluster octupole can be defined for all six domains and rotates every 60° within kagome planes. For the use of Mn_3Sn as antiferromagnetic spintronic materials, we need to manipulate such a TRS-broken domain structure by electrical means.

In sharp contrast with conventional antiferromagnets, there are two significant technical benefits in Mn_3Sn. First, we can use the external magnetic field to control the direction of the very weak remanent magnetization along the polarization axis of the cluster octupole moment[14,18]. Second, a topological response appears corresponding to the octupole configuration in the transport property, such as AHE[14,15]. Therefore, a similar experimental procedure used for ferromagnets can be applied to Mn_3Sn.

In this work, we have investigated the method for electrical manipulation of AFDWs in a microfabricated single-crystal Mn_3Sn. We observed the asymmetric magnetoresistance (AS-MR) effect[21] due to AFDW displacement in Mn_3Sn, which revealed that a submicrometer Bloch-like octupole domain wall is trapped parallel to kagome planes in-between the two pairs of electrodes. By using the above detection method, we have also demonstrated AFDW injection and subsequent displacement as a response to the local injection of electric current.

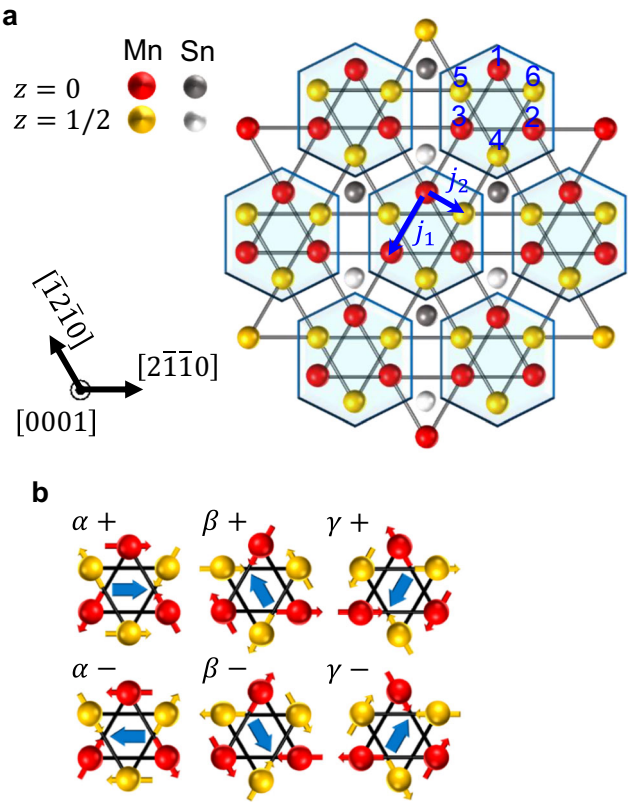

Fig. 1 Crystal and domain structure of Mn_3Sn. a Top view of the lattice structure for Mn_3Sn. Both Mn and Sn atoms are depicted with different colors between those in the $z = 0$ and 1/2 plane. Blue-colored hexagonal areas indicate units of octupole moments shown in Fig. 1b. Each Mn moment at overlapping two triangular sublattices is labeled with "1–6". The exchange integrals are illustrated by blue arrows between the closest Mn moments in the same sublattice (j_1) and the neighboring kagome planes (j_2), respectively. **b** Six types of cluster octupole moments consisting of two kagome triangles between neighboring layers[18,20]. The octupole moment parallel to a very small remnant magnetization is illustrated by blue arrows.

Results

Electrical detection of AFDWs. Figure 2a shows the scanning electron microscope image of the sample for detecting AFDW by magnetoresistance measurements. The four pairs of detection electrodes 1–5, 2–6, 3–7, and 4–8 were attached to a μm-scale Mn_3Sn rectangular plate perpendicular to the [0001] direction, besides current injection pads (I_+, I_-) connected parallel to the [0001] direction. The external magnetic field **H** was applied along the $[01\bar{1}0]$ direction perpendicular to the sample plane to make the antiferromagnetic single-domain state. Figure 2b, c presents the typical longitudinal magnetoresistance curves performed by using two different pairs of electrodes (6–7 and 2–3), where red (blue) symbols indicate the results for the positive (negative) field sweep. For the measurements using electrodes 6–7 (Fig. 2b), a hysteretic dip (peak) structure appeared in the magnetoresistance ρ_{67} for the positive (negative) sweep around H ~+3200 Oe (−3100 Oe).

For the measurement by using electrodes 2–3 (Fig. 2c), on the other hand, a peak (dip) in the magnetoresistance ρ_{23} appeared around the positive (negative) coercivity for the positive (negative) sweep. Such odd responses in the longitudinal magnetoresistance originate from the AS-MR effect known for large AHE materials[21]. The schematic image of the AS-MR is given in cases (i) and (ii) in Fig. 2e. The oppositely aligned cluster

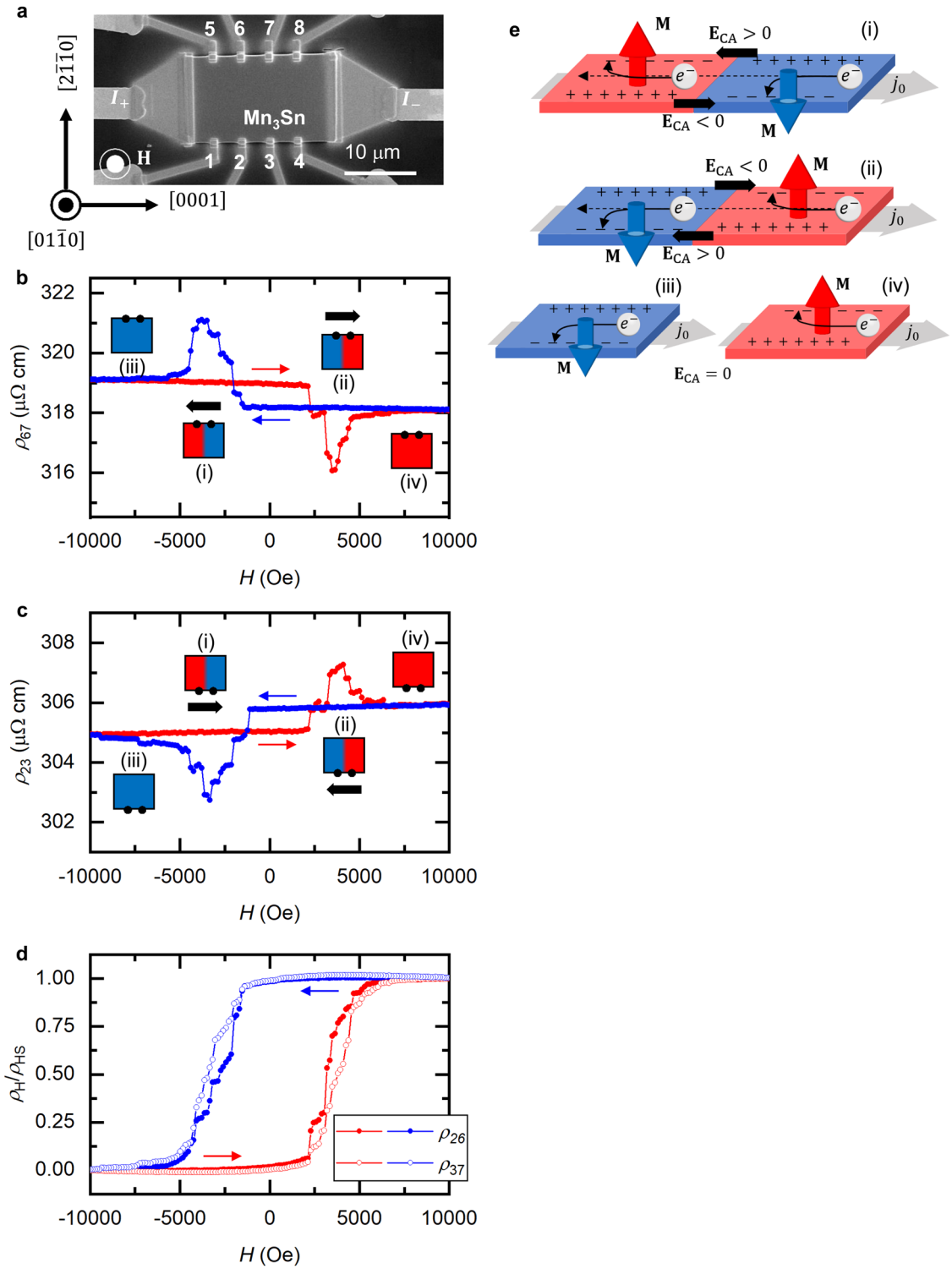

Fig. 2 Electrical detection of antiferromagnetic domain walls (AFDWs) for Mn_3Sn. a The scanning electron microscope (SEM) image of the sample used for detecting AFDWs by the asymmetric magnetoresistance (AS-MR). The detection current flows to the [0001] direction and the external field is applied to the [01$\bar{1}$0] direction. **b**, **c** The longitudinal measurements using the electrodes 6–7 (ρ_{67}) and 2–3 (ρ_{23}). **d** The transverse Hall measurements using the electrodes 2–6 (ρ_{26}) and 3–7 (ρ_{37}) normalized by the high field saturation value ρ_{HS} ($|H|$ =1.1 T). The red symbols and arrow present positive sweep, while the blue ones present negative sweep. Inset illustrations (i)–(iv) present the corresponding domain configurations under each field; the red region indicates $\beta+$ domain, whereas the blue region indicates $\beta-$ domain in Fig. 1b. **e** The schematic of AS-MR emerged across the domain wall for materials with large anomalous Hall conductivity, for given domain configurations of (i)–(iv) in Fig. 2b, c. The error bars are much smaller than the data point and are not presented.

octupole moment **M** in the antiferromagnetic Mn_3Sn, across the domain wall, causes opposite Hall conductance. In such a case, the AHE gives rise to the steady charge accumulation in the vicinity of the domain walls, resulting in effective electrical fields $\mathbf{E}_{CA}$ across the domain wall. The sign of $\mathbf{E}_{CA}$ is opposite to each other between the upper and lower edges, causing an odd response in the magnetoresistance effect between the top (6–7) and bottom (2–3) electrodes.

These results, in other words, indicate that AFDW moves along the [0001] direction during the field- sweeping process. Figure 2d, the transverse Hall resistivities ρ_{26} and ρ_{37} normalized by the high field saturation value ρ_{HS} ($|H| = 1.1$ T), supports the above hypothesis. The switching field of the left-hand side ρ_{26} is always smaller than that of the right-hand side ρ_{37}. Furthermore, the field range where the AS-MR takes place coincides well with the range where the difference in switching field is present between ρ_{26} and the above experimental facts, indicating that the domain wall propagates from left to right along the [0001] direction, and the AS-MR behaviors are triggered when the domain wall propagates between the electrode pairs.

The insets of Fig. 2b, c correspond to four kinds of the domain configurations (i)–(iv) in Fig. 2e at a given field, where the red region indicates the region of positive cluster octupole moment ($\beta+$ domain in Fig. 1b). At the same time, the blue one presents a negative moment ($\beta-$ domain). For example, in case of (ii), the dip (peak) under the positive field in the top (middle) panel is attributable to the positive (negative) $\mathbf{E}_{CA}$ appearing at the top (bottom) edge across $\beta-$ and $\beta+$ domains. The sign of E_{CA} is presented by a tiny arrow at the top or bottom of the domain illustration. The peak (dip) under the negative field can be understood in the same manner by switching $\beta+$ and $\beta-$ domains. Our setup with 4-μm-separated electrodes indicates that the length of an AFDW between these $\beta-$ and $\beta+$ domains would be shorter than this separation distance. The MOKE measurements[19] also revealed that the AFDW appeared in-between $\beta+$ and $\beta-$ domains, but its precise dimension and the microscopic spin texture have been difficult to be detected experimentally using our μm-scale devices. We then have investigated the atomistic numerical calculation to access the fine details of the AFDW, which will be introduced in the last section of this report.

Electrical nucleation of AFDWs. Based on the above insights, we have next performed experiments using the wedge-shaped Mn_3Sn device with thickness variation along the [0001] direction, as shown in Fig. 3a, to demonstrate AFDW nucleation by the pulse-current injection. Such a thickness profile enables the sharp domain switching by field sweep, as shown in Fig. 3b, in contrast to the multistep switching of Fig. 2d. The five pairs of electrodes along the [0001] direction can monitor longitudinal resistivities, ρ_{910}, ρ_{45}, and ρ_{15} in the same manner as the demonstration in Fig. 2.

Figure 3c shows the field dependence of ρ_{15} along the $[01\bar{1}0]$ direction. As is expected from the sharp switching in this sample, we observe no positive or negative hump unique to AS-MR near the coercive field (~1200 Oe), indicating that no AFDW nucleates during the switching process. Next, we injected a current pulse between the electrodes 10–5 with the current density of 3.9×10^9 Am^{-2} and the duration of 50 ms, to induce the local AFDW nucleation. Figure 3d, e exhibits field dependences of ρ_{910} and ρ_{45} after the current pulse injection. We set the external field at +860 Oe during the pulse injection to assist the AFDW nucleation and then decreased down to +420 Oe in order not to wipe out the injected AFDW during the measurement. The above ρ vs. H curves comprise the ascending (positive) sweep from +420 Oe to +10,000 Oe (red symbols) and the descending (negative) sweep from +420 Oe to −10,000 Oe (blue symbols). The negative jump takes place around 740 Oe ≤ H ≤ 1200 Oe for ρ_{910}, while the positive step appears in the same field region for ρ_{45} during the positive sweep. Besides, no jump appears in a magnetoresistance during the negative sweep. These odd behaviors in magnetoresistance are unique to AS-MR, assuring a successful injection of AFDW along the kagome planes at the electrodes 10–5.

The typical threshold current density for the AFDW nucleation is $j_t \sim 10^9$ A m^{-2} under $H = 100$–1000 Oe, which is about two orders of magnitude smaller than the typical values $j_{t,FM} \sim 10^{11-12}$ A m^{-2} for ferromagnets[22] and $j_{t,SOT} \sim 10^{11}$ A m^{-2} for spin–orbit torque-induced switching in CuMnAs[6]. The small j_t maybe characteristic of the antiferromagnetic nature of Mn_3Sn, where the noncollinear spins may rotate with small cost of additional magnetic energy owing to the spin frustration at kagome triangles[23], compared with the switching of the collinear ferromagnetic nature. Further investigation is necessary for quantitative comparison with previous results of the spin torque-induced switching.

The schematic insets in the figure correspond to the domain configurations, as in the cases of Fig. 2b, c. The shape of the AS-MR peak/dip in Fig. 3d, e appears more rectangular than multilevel peak/dip structures in Fig. 2b, c. This apparent difference indicates that the confined domain wall in Fig. 3d, e experiences less pinning potentials than in Fig. 2b, c, reflecting the smooth switching process due to the wedge profile, where the thickness variation induces a potential gradient of AFDWs along the [0001] slope direction.

Electrical displacement of AFDWs. We fabricated a device for the current pulse injection measurement as shown in Fig. 4a to nucleate a straight AFDW in a more controlled manner similar to the conventional experiment in ferromagnetic nanowires[24,25]. We also add a wedge-shape variation in the wire thickness to initiate a sharp domain wall propagation identical to the situation in Fig. 3a. The sample has two Hall bars labeled as probes 1 and 2, where probe 1 is for injection, while probe 2 is for detection, respectively. The assisting perpendicular field of +860 Oe is applied along the $[01\bar{1}0]$ direction during the whole experimental process.

First, we have investigated the AHE response to the current-induced nucleation process of the AFDW by applying a 50-ms pulse current with $j = +7.2 \times 10^9$ A m^{-2} along the $[2\bar{1}\bar{1}0]$ direction. Figure 4b shows a successful domain-switching process observed as an evolution of the Hall resistivity at probe 1 (ρ_{H1}) normalized by the saturation field $|H| = 1.1$ T (ρ_{HS1}), as ρ_{H1}/ρ_{HS1}. After injecting the 20th pulse current, the value of ρ_{H1}/ρ_{HS1} jumps up to 1.0, indicating that the $[01\bar{1}0]$ oriented $\beta-$ cluster octupole domain at probe 1 entirely flipped to the $\beta+$ domain[26].

Once the switching is complete, there are a pair of AFDWs nucleated at the intersection of probe 1 and a horizontal wire along the [0001] direction. The application of the second pulse current drives the AFDW toward probe 2 that detects the AHE signal as a function of the pulse duration, giving information about the evolution of AFD configuration. Before starting the second pulse experiment, we have checked whether the pulse current could nucleate an additional domain or not. Figure 4c presents the normalized Hall resistivity at probe 2 ρ_{H2}/ρ_{HS2} after the application of the second pulse but without the first pulse. The value of ρ_{H2}/ρ_{HS2} remained unchanged with the average current densities $j_a \leq (9.7 \pm 0.1) \times 10^9$ A m^{-2}, assuring that the second pulse itself nucleates no additional AFDW. Therefore, we set the current density below the above value for the following experiments.

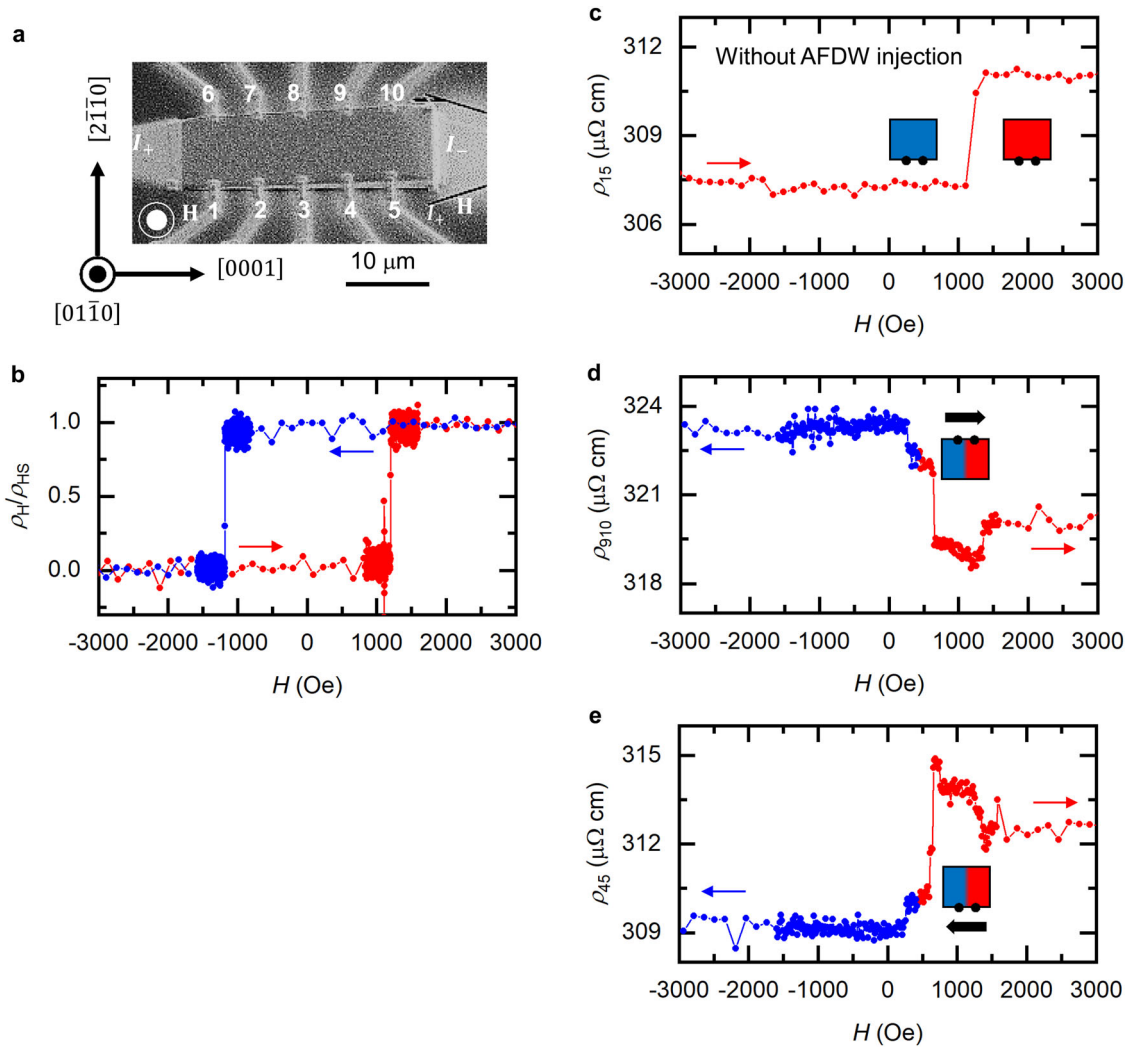

Fig. 3 Current-induced injections of antiferromagnetic domain walls (AFDWs) for Mn_3Sn. a The scanning electron microscope (SEM) image of the sample used for AFDW injections by pulse currents. The detection current flows to the [0001] direction and the external field is applied normal to the plane. **b** The normalized transverse Hall measurement using the electrodes 5-10 (ρ_H/ρ_{HS}). The red symbols present positive sweep (−10,000 Oe to +10,000 Oe), while the blue ones present negative sweep (+10,000 Oe to −10,000 Oe). **c** The longitudinal measurements using the electrodes 1-5 (ρ_{15}) without pulse injections. The external field is swept from −10,000 Oe to +10,000 Oe. **d**, **e** asymmetric magnetoresistance (AS-MR) measurements after the pulse injection using the electrodes 9-10 (ρ_{910}) and 4-5 (ρ_{45}). The red symbols and arrow present positive sweep from $H = +420$ Oe to $H = +10{,}000$ Oe, while the blue ones present negative sweep from $H = +420$ Oe to $H = -10{,}000$ Oe. The pulse currents with the current density of 3.9×10^9 A m^{-2} and the duration time of 50 ms were injected using the electrodes 10–5 under the assisting field $H = +860$ Oe along [01$\bar{1}$0] direction. Inset illustration presents corresponding domain configurations under each field; the red region indicates $\beta+$ domain, whereas the blue region indicates $\beta-$ domain in Fig. 1b. Bottom panel: the error bars are much smaller than the data point and are not presented.

Figure 4d shows the normalized anomalous Hall resistance ρ_2/ρ_{HS2} at probe 2 as a function of the pulse duration time D_t, i.e., an AFDW propagation time. We chose three different current densities J_a relative to the depinning threshold current density $j_c = 4.5 \times 10^9$ A m^{-2}, $j_a = +(6.7 \pm 0.3) \times 10^9$ A m^{-2} > $|j_c|$ (solid symbols), $j_a = -(6.7 \pm 0.3) \times 10^9$ A m^{-2} < $-|j_c|$ (open symbols), and $j_a = +(4.3 \pm 0.2) \times 10^9$ A m^{-2} < $|j_c|$ (green symbols), respectively. An abrupt ρ_2 jump took place only when injected current density exceeded its depinning threshold ($j_a > |j_c|$ or $j_a < -|j_c|$). These experimental facts assure that the injected AFDW can propagate toward probe 2 in response to the second pulse injection. This behavior is similar to the case for the ferromagnetic nanowires[24,25]. Therefore, the value of D_t at the jump must be the traveling time of the AFDW, ΔD_{t0}, and the propagation velocity v_{DW} can thus be given by $v_{DW} = L/\Delta D_{t0}$ with the separation distance L of two Hall probes. The estimated v_{DW} is plotted as a function of j_a in Fig. 4e.

Since the potential energy U of the AFDW scales with the cross-sectional area of the Mn_3Sn wire, the wedge shape induces a potential gradient ΔU along the slope in the [0001] direction, resulting in a unidirectional propagation from the thicker to the thinner region with the positive velocity ($v_{DW} > 0$), as shown in Fig. 4e. This situation indicates that the potential gradient is larger than the pinning forces of the distributed pinning centers along the slope. The propagation of the AFDW is thus like the creep type[27] whose propagation velocity $v_{DW} \sim v_{creep} = v_0 \exp\left[-\frac{U_C}{kT}\left(\frac{f_C}{f}\right)^{-\mu}\right]$. Here, U_C is the pinning potential due to disorders, f the driving force, and f_C the threshold force. Our results are nicely fit to the above equation, as indicated by the black dotted

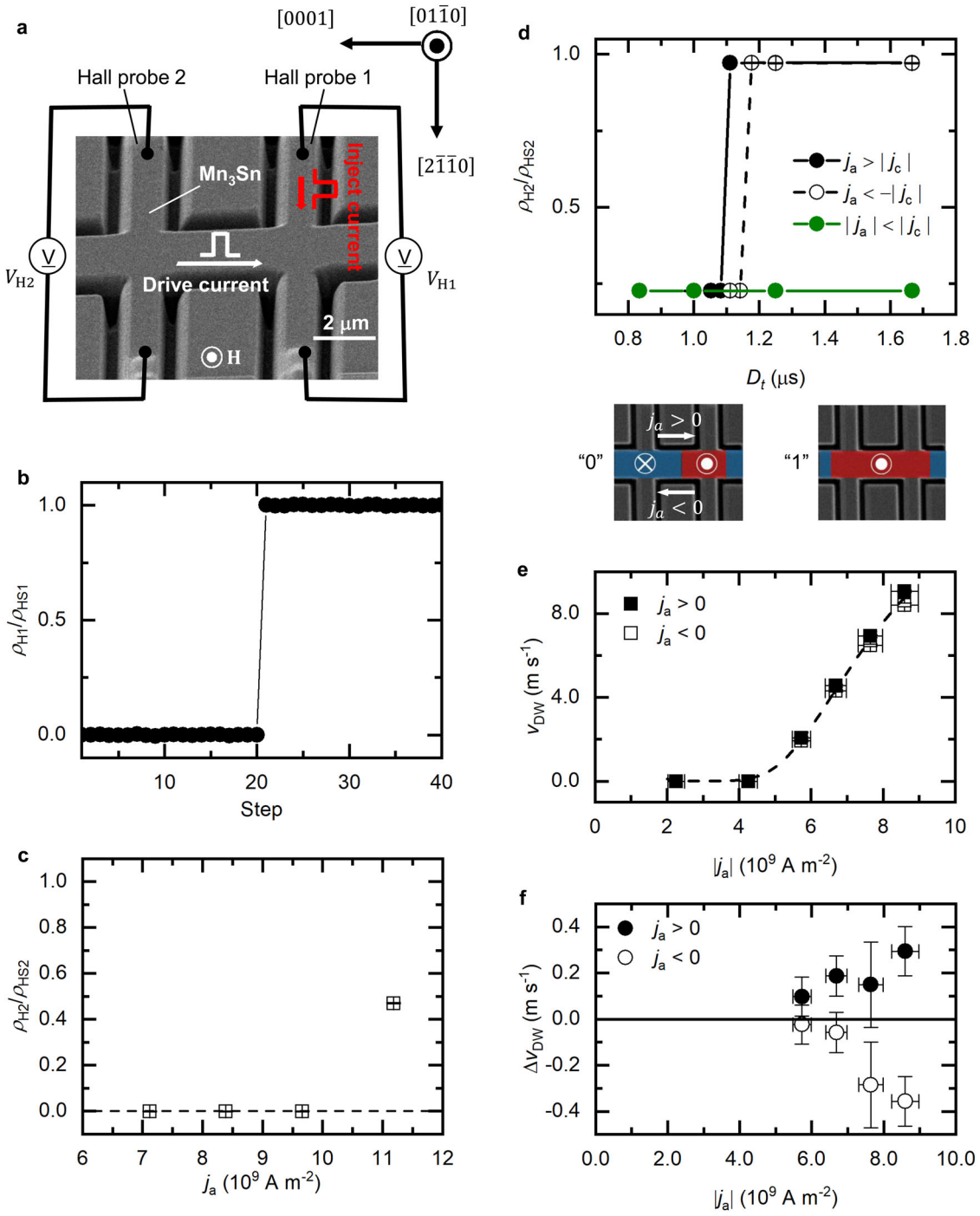

Fig. 4 Current-induced propagation of antiferromagnetic domain walls (AFDWs) for Mn_3Sn. a The scanning electron microscope (SEM) image together with the schematic diagram for domain wall injection/driving experiments. An antiferromagnetic domain is generated at the right Hall probe 1 by the injection pulse current along [2$\bar{1}\bar{1}$0] direction, and then driven by the pulse current along [0001] direction. Subsequent anomalous Hall measurement at Hall probe 2 monitors whether the injected domain has reached probe 2 or not. **b** AFDW injection event detected by the Hall probe. The direction of the octupole moment is identified via normalized Hall resistivity at Hall probe 1, ρ_1/ρ_{HS1}. **c** The driving pulse-current density dependence of the normalized anomalous Hall resistivity at detection probe 2, ρ_2/ρ_{HS2}, without the injection pulse current. The pulse duration time is set to be 50 μs. **d** The total pulse duration time D_i dependence of the normalized anomalous Hall resistivity at Hall probe 2, ρ_2/ρ_{HS2}, for positive depinning current $j_a > |j_c|$ (black symbols), negative depinning current $j_a < -|j_c|$ (open symbols), and below depinning current $|j_a| < |j_c|$ (green symbols). Bottom insets illustrate domain configurations before ("0") and after propagation ("1"). The positive current $j_a > 0$, (negative current: $j_a < 0$) is set so that an electron e^- flows from Hall probe 1 (2) to probe 2 (1). **e**, **f** Current-density dependence of the raw AFDW velocity v_{DW} and its directional contribution Δv_{DW}. A dashed line in Fig. 4e indicates the fitting of thermally induced creep component v_{creep}. The error bars are much smaller than the data point and negligible, except for those in Fig. 4e, f.

line, yielding $\mu \approx 0.53$, indicating the contributions of the random-field disorder by Mn atoms[28]. Besides, we also observe the tiny current-polarity-dependent contribution in v_{DW} obtained from $\Delta v_{DW} = v_{DW} - v_{creep} \neq 0$, plotted in Fig. 4f. The finite Δv_{DW} implies the nontrivial current-induced contribution to AFDW propagation, except for heating and shape effects. The Δv_{DW} of 0.1–1.0 ms^{-1} under $j_a \sim 10^9$ A m^{-2} is very small, but it could linearly increase up to the order of 10–100 m s^{-1} at $j_a \sim 10^{11}$ A m^{-2}. Moreover, the Δv_{DW} *vs* j_a implies that the AFDW moves in the same direction as the electron flow. The physical origin of this nontrivial current-polarity dependence is not clear. We, however, speculate that the origin may be the Dzyaloshinskii–Moriya interaction attributed to weak ferromagnetism of Mn_3Sn[29], or a new class of spin torque exerting on the macroscopic cluster octupole moments in Mn_3Sn[18,30]. Further investigation is indeed necessary to achieve a robust conclusion.

Numerical calculation of AFD structure. For an in-depth understanding of the AFDW structure in the Mn_3Sn wire, we performed micromagnetic calculations based on an atomistic micromagnetic calculation[31], using the experimentally reported lattice constant of Mn atoms in kagome triangles. The motion of the spins at triangular sublattices in kagome planes is calculated by Landau–Lifshitz–Gilbert equation[32]

$$\partial_t \mathbf{m}_i = -\gamma \mathbf{m}_i \times \mathbf{H}_{\mathrm{eff}} + \alpha \mathbf{m}_i \times \partial_t \mathbf{m}_i (i = 1, 2, \ldots, 6) \quad (1)$$

solved by a fourth-order Runge–Kutta algorithm. Here, $\mathbf{m}_i$ is each sublattice moment of six manganese atoms, which consist of an octupole moment in Fig. 1a, and the damping constant α is set $\alpha = 1$ for quick energy minimization. The effective net field $\mathbf{H}_{\mathrm{eff}}$ is calculated by integrating the exchange field H^{exc}, the magnetic anisotropy field H^{K}, and Dzyaloshinskii–Moriya interaction (DMI) field H^{DMI}. We ignored the dipolar interaction between spins. We calculated above effective fields as the energy first derivative with respect to the octupole moment $\mathbf{M} = \sum_{i=1}^{6} \mathbf{m}_i$ as

$$H^{\mathrm{exc}} = -\frac{\delta \varepsilon^{\mathrm{exc}}}{\delta \mathbf{M}} \text{ with } \varepsilon^{\mathrm{exc}} = -\sum_{i \neq j} j_{ij} \mathbf{m}_i \cdot \mathbf{m}_j, \quad (2)$$

$$H_i^{\mathrm{K}} = -\frac{\delta \varepsilon_i^{\mathrm{K}}}{\delta \mathbf{m}_i} \text{ with } \varepsilon_i^{\mathrm{K}} = -K(\mathbf{n}_i \cdot \mathbf{m}_i)^2, \quad (3)$$

and

$$H^{\mathrm{DMI}} = -\frac{\delta \varepsilon_1^{\mathrm{DMI}}}{\delta \mathbf{M}} \text{ with } \varepsilon_1^{\mathrm{DMI}} = \sum_j D_{1j} \left(m_{1x} \cdot m_{jy} - m_{1y} \cdot m_{jx} \right). \quad (4)$$

The material parameters used in the simulation are the exchange integrals $j_{ij} = j_1 = -2.8$ meV per link for (i, j) in the same kagome plane, $j_{ij} = j_2 = -2.8$ meV per link for (i, j) in the neighboring kagome plane (Fig. 1a), the anisotropy constant along [0001] direction $K = K_{\perp} = -14$ meV per atom, and $[2\bar{1}\bar{1}0]$ direction $K = K_{\parallel} = 0.187$ meV per atom, the Dzyaloshinskii–Moriya constant $D_{1j} = 0.635$ meV $Å^{-1}$, the gyromagnetic ratio $\gamma = 1.76 \times 10^{11}$ $T^{-1}s^{-1}$, and the lattice constants $a = 5.363$ Å, $b = 4.327$ Å[20,23]. The calculation region in [0001], [1210], and $[2\bar{1}\bar{1}0]$ directions are 7.0895 μm, 5.363 Å, and 10.726 Å, respectively.

Figure 5 summarizes the calculation of the AFDW structure. Importantly, the calculation reproduces the weak remanent magnetization $\delta \mathbf{m} \sim 4 m \mu_B$ parallel to the octupole moment, resulting from the inverse triangular distribution of six Mn sublattice moments in Fig. 1b. These cluster octupoles with weak magnetization are essential to describe the calculated AFDW structure shown in Fig. 5a. The boundary condition for the

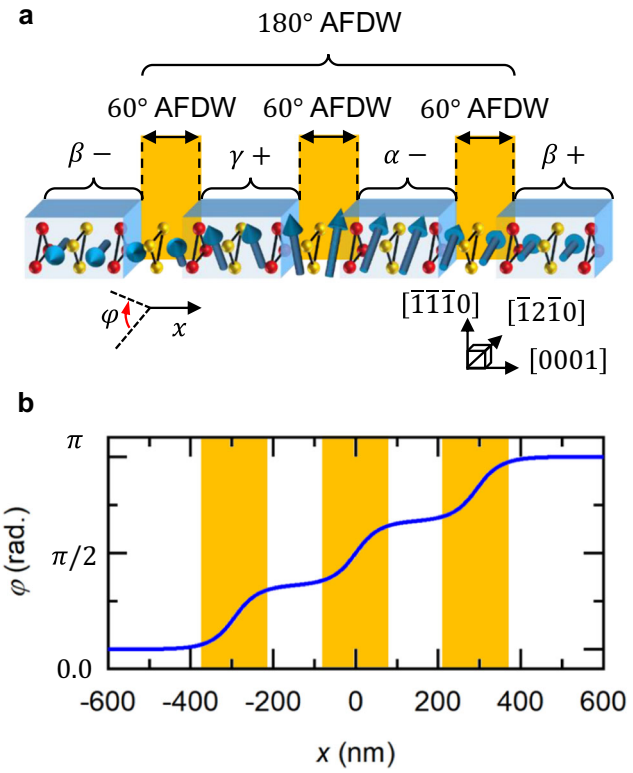

Fig. 5 Atomistic calculation results of antiferromagnetic domain walls (AFDWs) structures confined in Mn_3Sn. a An illustration of a calculated 180° antiferromagnetic octupole domain wall for Mn_3Sn. The entire 180° AFDW structure can be divided into three segments of 60° AFDWs sandwiched by four antiferromagnetic domains, those octupole moments rotating along the *x*-axis ([0001] direction) with the rotation angle φ. **b** Calculated profile of the octupole moment φ along the *x*-axis. The octupole moments gradually rotate between neighboring kagome planes, forming stepwise Bloch domain wall configuration.

calculated AFDW is a 180° rotation of the octupole moment along the [0001] direction. The AFDW consists of four AFDs, $\beta+$, $\alpha-$, $\gamma+$, and $\beta-$ with three 60° AFDWs in-between neighboring AFDs, as shown in Fig. 1a, b. As can be seen in Fig. 5b, the overall AFDW structure exhibits the stepwise rotation over 180°. We call this type of AFDW structure, "Bloch-like 180° AFDW". The thicknesses of each AFD and 60° AFDW are, respectively, ~120 and ~185 nm, yielding approximately 800 nm for the entire Bloch-like 180° AFDW.

Discussion

Such sub-μm domain wall should be detectable by optical means as already reported in a MOKE study[19]. Our μm-scale devices have enough space resolution to monitor the whole 180° AFDW as discussed in Figs. 2–4, but should be difficult to detect each 60° AFDW separately. Further fine processing down to 100–10-nm scale would enable to discuss such stepwise AFDW profiles by electrical means, to be observed via AHE and AS-MR.

In summary, we have investigated magnetotransport properties for a chiral antiferromagnet Mn_3Sn and developed an electrical means to control sub-μm size AFDWs. The AFDWs for Mn_3Sn consist of three Bloch-type domain walls sandwiched by four different domains, and their positions can be detected by the AS-MR effect. We have demonstrated that the current pulse injections can nucleate and displace these

domains. Interestingly, the introduction of the wedge shape turns out to be a practical means to induce smooth propagation of straight AFDW. These results could provide useful insights for the memory application in noncollinear antiferromagnetic spintronics.

Methods

Bulk preparation. Polycrystalline samples were made by melting the mixtures of manganese and tin in an alumina crucible sealed in an evacuated quartz ampoule in a box furnace at 1050 °C for 6 h. In preparation for single-crystal growth, the obtained polycrystalline materials were crushed into powders, compacted into pellets, and inserted into an alumina crucible that was subsequently sealed in an evacuated silica ampoule. Single-crystal growth was performed using a single-zone Bridgman furnace with a maximum temperature of 1080 °C and growth speed of 1.5 mm h^{-1}.

Devise fabrication. Single crystals were polished down to sub-mm pieces. Then, micro-Hall bars were fabricated by using a focused ion beam equipment (Scios DualBeam, Thermo Fisher Scientific Ltd.). The original sub-mm bulk pieces were formed into sub-μm thin plates by Ga+ ion beam accelerated by 5–30 kV with the injection angle of 0–5°. Subsequently, these plates were mounted onto a Si/SiO_2 substrate and fixed by perpendicularly injected Ga+ ion beam. The size of a Mn_3Sn plate for AS-MR detection in Fig. 2a is 15 μm in its width and 500 nm in its thickness. The Mn_3Sn wedge-shaped plate for AFDW nucleation in Fig. 3a has a width of 10 μm and a thickness of the wedge varies from 500 nm to 1 μm along the [0001] direction. The Mn_3Sn Hall bars for current-induced displacement in Fig. 4a have a width of 2 μm, with 5 μm in separation from probe 1 to 2, and 1 μm in their probe widths. In addition, wedge slopes varied sample thickness from 500 nm at Hall probe 1 to 1 μm at probe 2. They were finally embedded in the transport measurement device by merging conventional lift-off techniques for Cu and Ti/Au electrodes and W deposition using a FIB apparatus.

AFDW nucleation process. We performed all the measurements at room temperature and initialized the Mn_3Sn spin configuration by a strong enough field, $H \sim -1.1$T along the $[01\bar{1}0]$ direction before starting the experiment. We have checked the Joule heating effect by monitoring the current amplitude dependence of AHE conductivity σ_H[15]. The estimated temperature increase by pulse-current injections is less than 40 K, indicating that our Mn_3Sn device is in the AFM phase during measurements.

The initial condition for nucleating an AFDW was $j = +7.6 \times 10^9$ A m^{-2} with $H = +860$ Oe along $[01\bar{1}0]$ direction for all the current-induced AFDW displacement experiments. This assisting perpendicular field of +860 Oe was kept constant during propagation process. Small offsets of $\rho_{H_2}/\rho_{HS_2} \sim 0.2$ before zero-duration times in Fig. 4d implied that the AFD at probe 2 was slightly reversed by the exchange coupling between each kagome plane. Since these offsets did not change after the pulse-current injection, we assumed that they did not affect the AFDW propagation process.

Data availability

The authors declare that the data supporting the findings of this study are available within the article and are available from the corresponding author upon reasonable request.

Received: 9 April 2020; Accepted: 3 June 2020;
Published online: 19 June 2020

References

1. Slonczewski, J. C. Current-driven excitation of magnetic multilayers. *J. Magn. Magn. Mater.* **159**, L1–L7 (1996).
2. Miron, I. M. et al. Current-driven spin torque induced by the Rashba effect in a ferromagnetic metal layer. *Nat. Mater.* **9**, 230–234 (2010).
3. Chernyshov, A. et al. Evidence for reversible control of magnetization in a ferromagnetic material by means of spin-orbit magnetic field. *Nat. Phys.* **5**, 656–659 (2009).
4. MacDonald, A. H. & Tsoi, M. Antiferromagnetic metal spintronics. *Philos. Trans. R. Soc. A* **369**, 3098–3114 (2011).
5. Železný, J. et al. Relativistic Néel-Order fields induced by electrical current in antiferromagnets. *Phys. Rev. Lett.* **113**, 157201 (2014).
6. Wadley, P. et al. Electrical switching of an antiferromagnet. *Science* **351**, 587–590 (2016).
7. Wadley, P. et al. Current polarity-dependent manipulation of antiferromagnetic domains. *Nat. Nanotechnol.* **13**, 362–366 (2018).
8. Bodnar, S. Y. et al. Writing and reading antiferromagnetic Mn_2Au by Néel spin-orbit torques and large anisotropic magnetoresistance. *Nat. Commun.* **9**, 348 (2018).
9. Krén, E., Paitz, J., Zimmer, G. & Zsoldos, É. Study of the magnetic phase transformation in the Mn_3Sn phase. *Phys. B* **80**, 226–230 (1975).
10. Kuroda, K. et al. Evidence for magnetic Weyl fermions in a correlated metal. *Nat. Mater.* **16**, 1090–1095 (2017).
11. Chen, H. et al. Manipulating anomalous Hall antiferromagnets with magnetic fields. *Phys. Rev. B* **101**, 104418 (2020).
12. Tomiyoshi, S. & Yamaguchi, Y. Magnetic structure and weak ferromagnetism of Mn_3Sn studied by polarized neutron diffraction. *J. Phys. Soc. Jpn.* **51**, 2478–2486 (1982).
13. Nagamiya, T., Tomiyoshi, S. & Yamaguchi, Y. Triangular spin configuration and weak ferromagnetism of Mn_3Sn and Mn_3Ge. *Solid State Commun.* **42**, 385–388 (1982).
14. Chen, H., Niu, Q. & MacDonald, A. H. Anomalous Hall effect arising from noncollinear antiferromagnetism. *Phys. Rev. Lett.* **112**, 017205 (2014).
15. Nakatsuji, S., Kiyohara, N. & Higo, T. Large anomalous Hall effect in a non-collinear antiferromagnet at room temperature. *Nature* **527**, 212–215 (2015).
16. Ikhlas, M. et al. Large anomalous Nernst effect at room temperature in a chiral antiferromagnet. *Nat. Phys.* **13**, 1085–1090 (2017).
17. Kimata, M. et al. Magnetic and magnetic inverse spin Hall effects in a noncollinear antiferromagnet. *Nature* **565**, 627–630 (2019).
18. Suzuki, M.-T., Koretsune, T., Ochi, M. & Arita, R. Cluster multipole theory for anomalous Hall effect in antiferromagnets. *Phys. Rev. B.* **95**, 094406 (2017).
19. Higo, T. et al. Large magneto-optical Kerr effect and imaging of magnetic octupole domains in an antiferromagnetic metal. *Nat. Photo* **12**, 73–78 (2018).
20. Liu, J. & Balents, L. Anomalous Hall effect and topological defects in antiferromagnetic Weyl semimetals: Mn_3Sn/Ge. *Phys. Rev. Lett.* **119**, 087202 (2017).
21. Cheng, X. M. et al. Antisymmetric magnetoresistance in magnetic multilayers with perpendicular anisotropy. *Phys. Rev. Lett.* **94**, 017203 (2005).
22. Hayashi, M. et al. Dependence of current and field driven depinning of domain walls on their structure and chirality in permalloy nanowires. *Phys. Rev. Lett.* **97**, 207205 (2006).
23. Cable, J. W., Wakabayashi, N. & Radhakrishna, P. Magnetic excitations in the triangular antiferromagnets Mn_3Sn and Mn_3Ge. *Phys. Rev. B* **48**, 6159 (1993).
24. Vernier, N., Allwood, D. A., Atkinson, D., Cooke, M. D. & Cowburn, R. P. Domain wall propagation in magnetic nanowires by spin-polarized current injection. *Europhys. Lett.* **65**, 526–532 (2004).
25. Yamaguchi, A. et al. Real-space observation of current-driven domain wall motion in submicron magnetic wires. *Phys. Rev. Lett.* **92**, 077205 (2004).
26. Núñez, A. S., Duine, R. A., Haney, P. M. & MacDonald, A. H. Theory of spin torques and giant magnetoresistance in antiferromagnetic metals. *Phys. Rev. B* **73**, 214426 (2006).
27. Lemerle, S. et al. Domain wall creep in an ising ultrathin magnetic film. *Phys. Rev. Lett.* **80**, 849 (1998).
28. Lee, J.-C. et al. Universality classes of magnetic domain wall motion. *Phys. Rev. Lett.* **107**, 067201 (2011).
29. Dmitrienko, V. E. et al. Measuring the Dzyaloshinskii–Moriya interaction in a weak ferromagnet. *Nat. Phys.* **10**, 202–206 (2014).
30. Nomoto, T. & Arita, R. Cluster multipole dynamics in noncollinear antiferromagnets. *Phys. Rev. Res.* **2**, 012045(R) (2020).
31. Thiaville, A., Nakatani, Y., Miltat, J. & Suzuki, Y. Micromagnetic understanding of current-driven domain wall motion in patterned nanowires. *Europhys. Lett.* **69**, 990–996 (2005).
32. Li, Z. & Zhang, S. Domain-wall dynamics and spin-wave excitations with spin-transfer torques. *Phys. Rev. Lett.* **92**, 207203 (2004).

Acknowledgements

We thank A.A. Nugroho for his technical support of bulk crystal synthesis, and T. Higo for his fruitful discussions. This work is supported by CREST (Grant number JPMJCR18T3), by Grant-in-Aid for Scientific Research on Innovative Area, "Nano Spin Conversion Science" (Grant numbers 26103001 and 26103002), by "J-Physics" (Grant numbers 15H05882 and 15H05883), and by JSPS KAKENHI (Grant numbers 15H05702 and 16H02209). The use of the facilities of the Materials Design and Characterization Laboratory at the Institute for Solid State Physics, The University of Tokyo, is gratefully acknowledged.

Author contributions

Y.O. and S.N. conceived the project. S.S. planned and S.S., T.T., M.I., and M.K. performed the experiments, and S.S. and Y.Y. analyzed the data. Y.N. performed the numerical calculation. S.S., Y.Y., K.K., S.N, and Y.O. wrote the main text.

Competing interests
The authors declare no competing interests.

Additional information
Correspondence and requests for materials should be addressed to Y.O.

Reprints and permission information is available at http://www.nature.com/reprints

Publisher's note Springer Nature remains neutral with regard to jurisdictional claims in published maps and institutional affiliations.